

## Article

# Simulated Docking Predicts Putative Channels for the Transport of Long-Chain Fatty Acids in *Vibrio cholerae*

Andrew Turgeson <sup>1,†</sup> , Lucas Morley <sup>2,†</sup>, David Giles <sup>3,†</sup>  and Bradley Harris <sup>1,\*,†</sup> <sup>1</sup> Department of Chemical Engineering, University of Tennessee at Chattanooga, Chattanooga, TN 37403, USA<sup>2</sup> Department of Biological Sciences, University of Pittsburgh, Pittsburgh, PA 15260, USA<sup>3</sup> Department of Biology, Geology, and Environmental Science, University of Tennessee at Chattanooga, Chattanooga, TN 37403, USA

\* Correspondence: bradley-harris@utc.edu; Tel.: +1-423-425-2209

† These authors contributed equally to this work.

**Abstract:** Fatty acids (FA) play an important role in biological functions, such as membrane homeostasis, metabolism, and as signaling molecules. FadL is the only known protein that uptakes long-chain fatty acids in Gram-negative bacteria, and this uptake has traditionally been thought to be limited to fatty acids up to 18 carbon atoms in length. Recently however, it was found *Vibrio cholerae* has the ability to uptake fatty acids greater than 18 carbon atoms and this uptake corresponds to bacterial survivability. Using *E. coli*'s FadL as a template, *V. cholerae* FadL homologs *vc1042*, *vc1043*, and *vca0862* have been computationally folded, simulated on an atomistic level using Molecular Dynamics, and docked *in silico* to analyze the FadL transport channels. For the *vc1042* and *vc1043* homologs, these transport channels have more structural accommodations for the many rigid unsaturated bonds of long-chain polyunsaturated fatty acids, while the *vca0862* homolog was found to lack transport channels within the signature beta barrel of FadL proteins.

**Keywords:** *Vibrio cholerae*; long-chain fatty acid transport protein; FadL; *vc1042*; *vc1043*; *vca0862*; *E. coli*; *b2344*; Molecular Dynamics; I-TASSER; AutoDock



**Citation:** Turgeson, A.; Morley, L.; Giles, D.; Harris, B. Simulated Docking Predicts Putative Channels for the Transport of Long-Chain Fatty Acids in *Vibrio cholerae*. *Biomolecules* **2022**, *12*, 1269. <https://doi.org/10.3390/biom12091269>

Academic Editor: Laurent Soulière

Received: 4 June 2022

Accepted: 1 September 2022

Published: 9 September 2022

**Publisher's Note:** MDPI stays neutral with regard to jurisdictional claims in published maps and institutional affiliations.



**Copyright:** © 2022 by the authors. Licensee MDPI, Basel, Switzerland. This article is an open access article distributed under the terms and conditions of the Creative Commons Attribution (CC BY) license (<https://creativecommons.org/licenses/by/4.0/>).

## 1. Introduction

In Gram-negative bacteria, the transport of exogenous long-chain fatty acids (LCFA) across the outer membrane leaflet is mediated by FadL [1–3]. FadL's ability to acquire LCFAs grants versatility in carbon source utilization, providing a selective advantage for survival. In the case of *Vibrio cholerae*, the causative agent of cholera, this bacterial robustness may have ecological and medical implications. In this paper, we will discuss the importance of bacterial FA synthesis and uptake. Then, we will compare novel structural models of *V. cholerae* FadL homologs with that of *E. coli*'s, highlighting both conservation and divergence in the proteins.

Fatty acids (FAs) are molecules with a carboxylic acid head group and an aliphatic tail group of varying length and saturation. FAs are used primarily as building blocks for cell membranes, but also supply energy and can be used as signaling molecules [4]. Fatty acids can be acquired from exogenous sources as well as being synthesized *de novo*. However, many organisms (such as *Homo sapiens*) require specific exogenous sources of FAs for specific metabolic functions [4]. In humans, this can be immune system regulation, blood clotting, neurotransmitter biosynthesis, cholesterol metabolism, and phospholipids for the brain and the retina [5].

In nature, plants typically have a limited synthesizing capacity that produces polyunsaturated fatty acids (PUFAs) up to only 18 carbons (many plants are still capable of monounsaturated and unsaturated FAs for waxes and seed storage lipids) [6]. However, plants are generally the only producers of n-3 ( $\omega$ -3) and n-6 ( $\omega$ -6) where the first unsaturated carbon starts on the 3rd or 6th carbon from the tail methyl group. Oddly, there are some

heterotrophic bacteria (*Vibrio* and *Pseudomonas*) that can also produce the typically plant based n-3 PUFAs [7]. Mammalian cells possess cytoplasmic fatty acid synthase (FAS), a major producer of 16-18 carbon atoms (which are also the most common cellular FAs in mammals) [6]. Typically, plants and animals do not create the higher order (>20 carbons) unsaturated fatty acids; instead, these longer chain FAs are commonly produced by marine protists and microalgae [6–8]. It is widely known that fish, mollusks, and crustaceans tend to have high concentrations of the longer chain FAs such as eicosapentaenoic acid (EPA, 20:5) and docosahexaenoic acid (DHA, 22:6) [5]. It is thought that all PUFAs in food webs originate from primary producers, where organisms further up the food chain have only the ability to modify the FA by bioconversion and elongation as they pass through the food web (i.e., trophic upgrading) [4]. Thus, fish, mollusks, and crustaceans that have a diet of microalga and protist have higher concentrations of the longer chain PUFAs, but have a lessened ability for FA conversion to long PUFAs than freshwater fish [4].

In bacteria, FAs are primarily used as components for the phospholipid bilayer of the membrane. These membrane phospholipids are constantly being synthesized, modified, recycled, and degraded to maintain membrane homeostasis and to respond to environmental stressors [9,10]. Free FAs are released during these processes, constituting important sources of metabolic energy [9]. Fatty acid biosynthesis involves a stepwise carbon elongation and unsaturation until the FA is of appropriate length and unsaturation. Further maintenance of membrane dynamics can be mediated by enzymes acting on constructed phospholipids, such as desaturases, cis/trans isomerases, and cyclopropane synthases [11].

Fatty acid synthesis pathways are highly conserved between bacteria and eukaryotes, the differences being the resulting fatty acids synthesized by bacteria tend to be slightly shorter, generally lack poly-unsaturation, and the monoenoic C18 acids have different double bond positions [12]. Bacteria use type II fatty acid synthesis (FASII), which starts with an acetyl-CoA carboxylase complex (ACC) interacts with a biotin-dependent enzyme catalyzing an irreversible carboxylation of acetyl-CoA to produce malonyl-CoA. The resulting malonyl-CoA is used for the elongation cycle which extends the growing fatty acid with consecutive reduction, dehydration, reduction and condensation reactions by various fatty acid biosynthesis (Fab) enzymes [6,13].

The elongation of an FA is costly, and as a result, all bacteria characterized to date have the capacity to uptake exogenous FAs [14]. The pathway for long-chain FA uptake in Gram-negative bacteria begins with the transmembrane protein FadL [2,15] to transport the FA into to periplasmic space, where it is then delivered through the inner membrane to FadD (acyl-CoA synthase or fatty acid-CoA ligase). FadD uses adenosine triphosphate (ATP) along with an FA, producing adenosine monophosphate (AMP) and  $P_2O_7^{-4}$  (PPi) and an FA bonded to a coenzyme A (CoA) [16]. The FA-CoA can then be shortened in beta oxidation producing a shorter FA tail and generating energy. Alternatively, an FA-CoA is the first component of an FAS elongation cycle, should the specific needs of the cell require a longer chain FA.

As previously stated, it was believed that enteric bacteria, such as *E. coli* and *V. cholerae*, were only able to acquire up to 18 carbon length FAs [17]. However, over the past decade several Gram-negative pathogens have been shown to assimilate and respond to exogenous PUFAs [18–21]. In the case of *V. cholerae*, this increased uptake is likely due to its natural ecosystem of tropical climates where marine algae and protist are the bases of the aquatic food web. The uptake of PUFAs allows the incorporation of these long-chain FA into the cell envelope, and this incorporation has been shown to affect the membrane permeability, motility, biofilm formation, and antimicrobial resistance of the bacterium [22]. Bile, along with mucus, in the human intestines has a large concentration of long-chain FAs in the form of phosphatidylcholine [23]. Consequentially, *V. cholerae* has a lysophospholipase protein (VolA *vca0863*) capable of cleaving phosphatidylcholine and liberating fatty acids for bacterial uptake [24].

With increasing attention towards FAs and their effects in biology, the study of a species that exhibits broader capacity for the uptake and use of FAs presents an opportunity

for comparison and elucidation of the uptake dynamics of the transmembrane protein FadL. In this paper, we study the predicted structure and functions of several *V. cholerae* FadL homologs (*vc1042*, *vc1043*, and *vca0862*) using Molecular Dynamics and perform comparisons to the *E. coli* (*b2344*) FadL homolog.

## 2. Materials and Methods

### 2.1. Selecting the *Vibrio cholerae* Homologs

*E. coli* M1655 FadL (accession number: NP\_416846) was used as input for a BLAST [25] homolog search against all available sequenced *V. cholerae* strains of the pathogenic O1 and O139 serogroups. The search algorithm settings were set at 100 max target sequences, short queries, an expect threshold of 10, a BLOSUM64 scoring matrix, with gap costs determined by Existence: 11 Extension: 1, and a Conditional composition score matrix adjustment. No filters or masks were used to analyze the results.

The resulting proteins were reduced to unique sequences and *vc1042*, *vc1043*, and *vca0862* (accession numbers: WP\_000856207, WP\_001061938, and WP\_000966057, respectively) were selected based on prevalence.

### 2.2. Generating the FadL Tertiary Structures

The selected *V. cholerae* sequences were removed of the predicted signal peptide sequences, folded using the I-TASSER [26] standalone version, and compared to the known crystal structure of *E. coli*'s FadL from the RCSB database (PDB ID: 1T16) [27]. The C-score determined by I-TASSER (on a scale from  $-5$  to  $2$ ) for *vc1042*, *vc1043*, and *vca0862* were  $0.58$ ,  $0.70$ , and  $-1.08$ , respectively. The resulting I-TASSER predicted structures can be seen in the Supplementary Material Figure S1. To validate the I-TASSER folded structures the homolog 111 sequences were then folded with AlphaFold [28] using the Colab server [29]. The resulting AlphaFold structures can be found in Figure S2. The resulting AlphaFold structures had PLDDT values typically above 90, indicating a very good prediction model. The lower scores were primarily still within acceptable tolerances, but these were typically found in the extracellular loops. A comparison between the I-TASSER and AlphaFold structures was performed by aligning each homolog and calculating the RMSD using VMD. The resulting aligned structures can be seen in Figure S3 and the RMSD for each homolog can be seen in Table S3. The extracellular loops appear to generate the largest difference between the I-TASSER and AlphaFold generated structures, and because these are suspected to have little involvement in the transport channels, the structures generated appear to have a good agreement. MolProbity [30] was used for a Ramachandran analysis of the I-TASSER and AlphaFold generated structures seen in Table S2.

### 2.3. Generating the Membrane System

The resulting computationally folded I-TASSER FadL structures, in addition to the *E. coli* *b2344* 1T16 crystal structure, were each placed into a membrane using the CHARMM-GUI Membrane Builder [31]. The *V. cholerae* homologs' membrane had an outer leaflet of *V. cholerae* type 1 Lipid A, Core A, and 15 O1 O-antigen units. The *E. coli* outer leaflet was composed of *E. coli* type 1 Lipid A, Core R1, and 3 *E. coli* O1 O-antigen units (with 5 sugars per O unit). Both types had an inner leaflet of 67% phosphatidylethanolamine (PE) and 33% phosphatidylglycerol (PG). The structure of each of these molecules can be seen in the Supplementary Material, Figure S4.

### 2.4. Equilibrating the Membrane Systems

The resulting simulation constraints generated by the CHARMM-GUI were then used in conjunction with NAMD [32] and CHARMM36 force fields [33]. During simulations, Langevin dynamics were used to maintain constant temperature (310 K) and pressure (1 atm). The simulations were sized as  $80 \text{ \AA} \times 80 \text{ \AA} \times 140 \text{ \AA}$  and a flexible cell boundary was chosen for an anisotropic membrane system. A cutoff of  $12 \text{ \AA}$  was used along with a particle mesh Ewald [34] for electrostatic interactions. All equilibrations used a timestep

of 2 fs and nonbonded frequency and full electrostatics calculated at every step. Each of the four protein systems were equilibrated for a minimum of 250 ns. The RMSD of the equilibration run for each protein tested can be seen in Figure S5. A Ramachandran plot was made to detect conformational outliers and determine a Z-score using MolProbity [30] of the homolog structures at 0 and 201 ns to determine the differences between structure of the and the initial and membrane equilibrated structures. The outlier residues found were sparse both spatially and numerically in both instances, indicating that the structures were of good agreement. Additionally, the Z-scores were within acceptable tolerances, where typically the absolute value being less than 2 (Table S2 in the Supplemental Material).

### 2.5. The Docking of the FadL Proteins

50 frames of the equilibrated FadL trajectories were taken (one every nanosecond) starting at 201 ns into the equilibration and ending at 250 ns. For each frame, the protein was isolated and aligned with respect to the 1T16 position. An array of 10 ligands (Table S1) were 152 then blindly docked to each of the frames generated from equilibration using AutoDock 153 [35] (in addition to 50 repeated instances of the 1T16 crystal structure) with the purpose to 154 map the channels and binding sites. The  $80 \times 80 \times 120$  AutoDockTools gridbox binding region 155 (closer to a  $40 \text{ \AA} \times 40 \text{ \AA} \times 60 \text{ \AA}$  box) was restricted to the upper extracellular region of the 156 FadL proteins encasing the majority of the FadL proteins. To maintain the cis structures of the FAs, the unsaturated double bonds of the ligands were kept rigid during docking. Each docking used a genetic algorithm with a population size of 150, a maximum number of evaluations of 2,500,000, and a maximum of 27,000 generations.

To test the viability of AutoDock, we also docked 50 repeated instances of 1T16 using GNINA [36] with the same array of 10 ligands used with AutoDock. The autobox was produced using the entire protein, and the exhaustiveness was set to 64 to account for the large search space. The default CNN was used for rescoring the poses, and 10 poses were generated per ligand per frame.

The nodal cluster analysis was performed by using an in-house mean shift algorithm script written in VMD's TCL to locate the positions of the highest density of docked FAs. The mean shift algorithm propagated spheres (or nodes) with a radius of  $7 \text{ \AA}$  every  $7 \text{ \AA}$  in the x, y, and z directions, thus covering the entire volume of the system. The coordinates of any FA heavy atoms found within the sphere were averaged and the next iteration of the sphere started at the averaged coordinates. If a sphere did not have any heavy atoms, it was removed. The iterations stopped when the sphere movement stopped, usually around 10 iterations total. Overlapping sphere locations were combined and outliers, generated from stray docked FAs, were removed except in the case of Node 3 for homolog *vc1043* because the node was located in the S3 kink.

FAs were ascribed to the nodes based on proximity. Because the nodes represent docking locations of ambiguous size, the nodal spheres' radius were increased iteratively and any FA within the node's iterative radius was ascribed to that node.

## 3. Results

### 3.1. Docking Showed Viability between the Crystal Structure and Simulated results

Currently, there are no experimentally determined X-ray or NMR structures of the *Vibrio cholerae* FadL homologs, consequentially to find the structures of *vc1042*, *vc1043*, and *vca0862*, the protein sequences were computationally folded using I-TASSER to predict their native tertiary structures. Simulations were initiated from the computationally predicted structures with the Molecular Dynamic (MD) simulator NAMD along with the known structure of *E. coli*'s FadL *b2344* henceforth referred as *b2344*. Various conformations of the equilibrated structures were docked with AutoDock using an array of fatty acids shown in Figure 1.

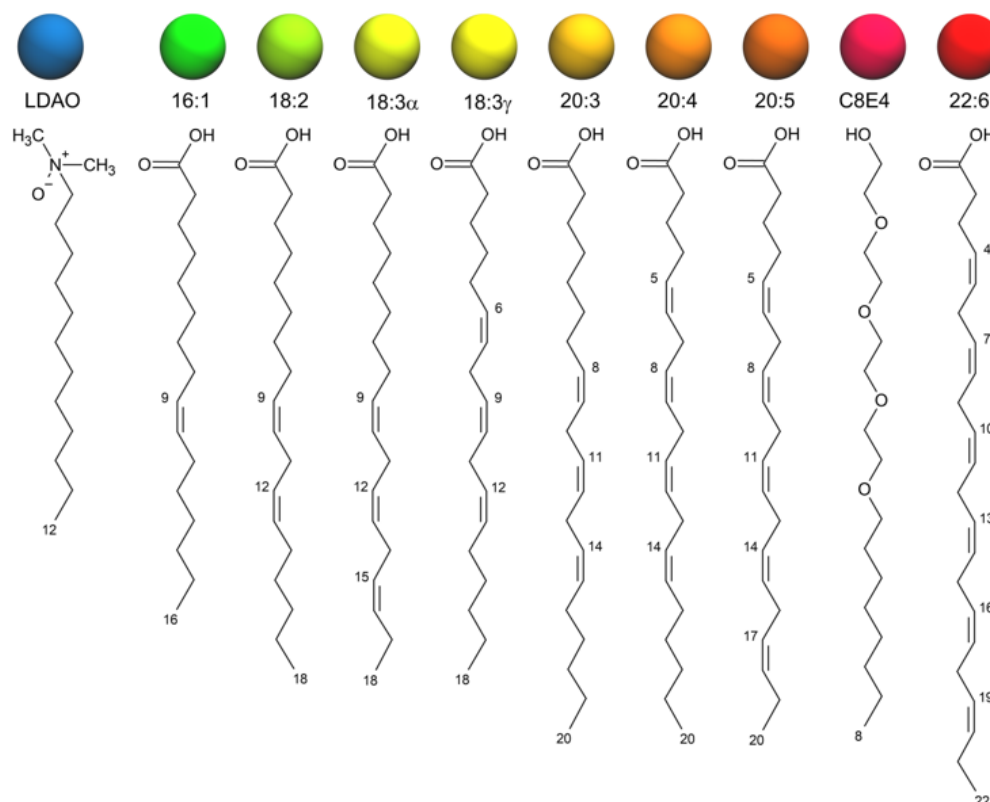


**Figure 1.** Fatty acids and detergents (LDAO and C8E4) used in docking the FadL homologs. The colored spheres show the color scheme associated with the corresponding fatty acid for images used throughout the paper.

To test the accuracy of the simulated docking, we compared the detergent binding from our simulated docking and the experimentally determined binding locations from van den Berg's crystallography study [27]. Specifically, using the *E. coli* FadL *b2344* crystal structure (1T16) was docked using AutoDock with LDAO and C8E4 as the ligands. The resulting simulated docking locations were compared with the experimentally determined bindings for LDAO and C8E4 molecules found in the 1T16 PDB structure. Figure 2 examines a frame of the resulting dockings showing a preference of the AutoDock bindings sites to primarily be the locations that were bound experimentally [27]. However, the selected docking of the S3 kink binding site (residues highlighted in green) contains C8E4 molecules where in the original crystal structure C8E4 molecules were restricted to the low affinity binding site in the L3 and L4 extracellular loops. This is likely due to the methodology of van den Berg, where LDAO and C8E4 competed for binding during the protein washing phase [27], while in simulated docking there was no binding competition.

### 3.2. Nodal Cluster Analysis Shows Agreement with Experimental Studies

Figure 3 shows the original *b2344* 1T16 crystal structure with the native detergents outlining the low affinity binding site, the high affinity binding site, and the S3 kink [27]. The AutoDock binding within the 1T16 crystal structure in conjunction with the mean shift algorithm did find that the docked FAs were located in the low affinity binding site (Node 1), the high affinity binding site (Node 2), and the S3 kink (Node 3).

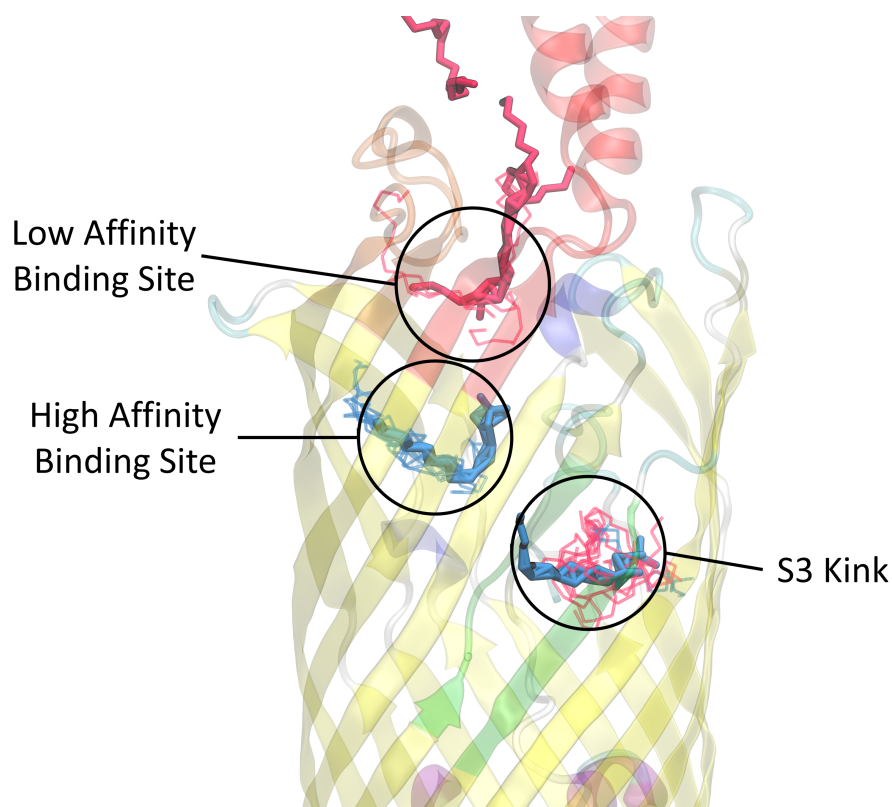


**Figure 2.** Docking of 1T16 with LDAO and C8E4 (lines) compared with the original LDAO and C8E4 (solid) placement from X-ray crystallography. While this is only one frame, the LDAO from docking tends to be strongly correlated to the crystallography bound LDAO, found in the high affinity binding site. The docked C8E4 was found to correspond to the crystallography bound C8E4 in the low affinity binding site, but the docked C8E4 was also found to bypass the transport channels and appear docked around the crystallography bound LDAO found the S3 kink. This occurrence is likely an effect of AutoDock's ligand placement algorithm and non-competitive docking). The L3 loop is colored red, the L4 loop is colored orange, and the S3 kink is colored green for reference.

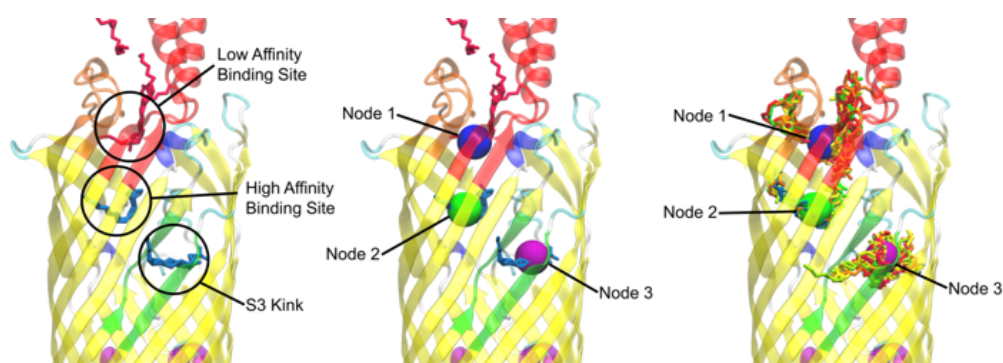


**Figure 3.** Mean shift based nodal analysis of the unequilibrated *b2344* (RCSB ID 1T16) docking. **(Left)** the original detergents from the 1T16 X-ray structure and locations of the low affinity binding site, the high affinity binding site, and the S3 kink as described by van den Berg [27]. **(Center)** The location of the nodes found by the mean shift algorithm from computationally docked FAs, the 1T16 crystal structure bound detergents are also shown to validate nodal locations. **(Right)** Nodal locations and a snapshot of FA clusters from docking that the mean shift algorithm used to generate the nodes showing relatively good correlation.

### 3.3. AutoDock Docking Compared to GNINA Docking

We compared the generated dockings of AutoDock with that of a similarly run GNINA docking for the experimentally found 1T16 structure (Figure 4). The nodal clusters were compared and found to be in good agreement with the high affinity binding site and S3 kink. There was some disagreement in the low affinity binding site locus (Node 1) being set closer to the extracellular space with GNINA than AutoDock, however, both these sites yielded ligand binding results that mirrored the X-ray crystallography results.

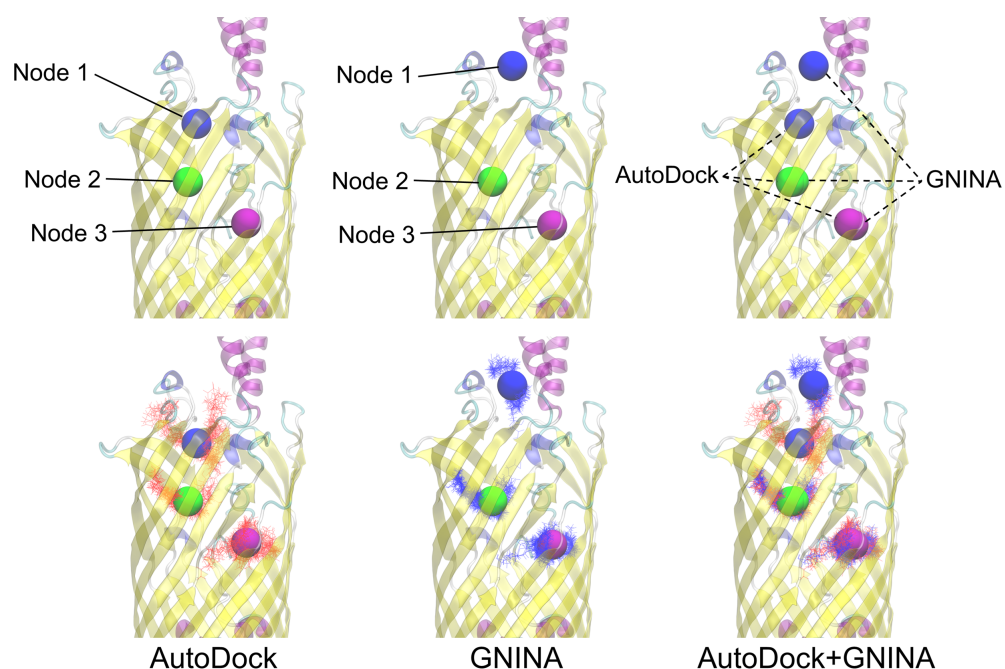


**Figure 4.** Nodal locations for AutoDock and GNINA. The nodes are labeled (**top**) and the ligands are represented for AutoDock (red) and GNINA (blue) in lines (**bottom**). Both sets of dockings appear to find the important nodes of the S3 kink and the high and low affinity binding sites. GNINA's docking did reveal a preference for the dockings to be located closer to the extracellular space than AutoDocks, but the C8E4's binding from experimentation are still in close proximity.

A closer look at the ligand binding results shows a satisfactory level of agreement between the two methods. While in different proportions, typically, the longer chained ligands tend to be found less in the high affinity binding site (Node 2) and more in the other sites (Figure 5). However, GNINA tends to propagate more of the tested ligands in the high affinity binding site (Node 2) than AutoDock overall. This can likely be attributed to differences in the sampling method for each approach. One noteworthy difference from the GNINA docking was that, out of the 500 poses for the C8E4 ligands, none were found bound to the low affinity binding site. This is somewhat surprising as C8E4 was originally bound to the low affinity binding site (Node 1) in the 1T16 crystallography structure. This could possibly be due to the marked differences in the structure of the extracellular loops between the two methods. These differences could be particularly impactful for C8E4 due to non-favorable interactions between its hydrophilic headgroup and the hydrophobic residues of the low affinity binding site.

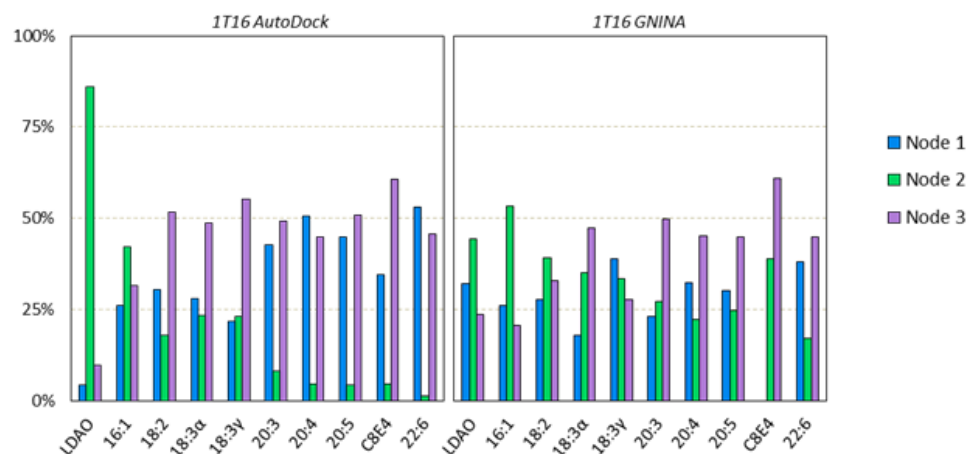


**Figure 5.** Charts of the percent of each ligand in proximity to each node between the AutoDock and GNINA dockings. Node 1 represents the low affinity binding site, Node 2 the high affinity binding site, and Node 3 the S3 kink. There were a total of 500 poses per ligand type docked.

### 3.4. Nodal Cluster Analysis Shows Ligand Preference for Certain Binding Sites

The mean shift nodal analysis was performed for each of the FadL and *V. cholerae* and the equilibrated *b2344* homolog structures, resulting in the nodal locations seen in Figure 6. The nodes from equilibrated *b2344*, Figure 6A, shows almost identical nodal locations as the X-ray 1T16 structure Figure 3. A small difference between the high affinity binding site where Node 2 tended to be closer to the center of the FadL beta barrel in the equilibrated structure). Exception aside, this demonstrates the NAMD equilibration *b2344* FadL structure tended to retain important structures during the simulation.

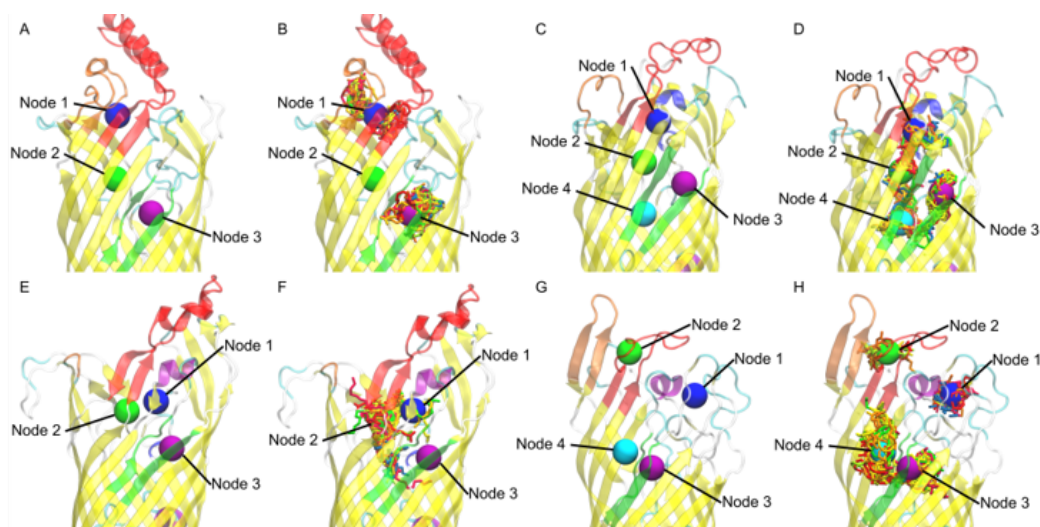


**Figure 6.** Nodal locations of: (A) *E. coli b2344*; (C) *vc1042*; (E) *vc1043*; (G) *vca862*. Example frame of FA clusters versus mean shift generated nodes for: (B) *E. coli*; (D) *vc1042*; (F) *vc1043*; (H) *vca862*.

### 3.5. The Nodal Analysis Shows Preference for Certain Node Loci

The FAs were categorized based on proximity, with each docked FA being prescribed one node per frame. With 10 FAs per type per frame and 50 frames, 5000 FAs were assigned to each FadL homolog—giving a reasonable statistical model. The resulting docked locations were summarized in Figure 7.



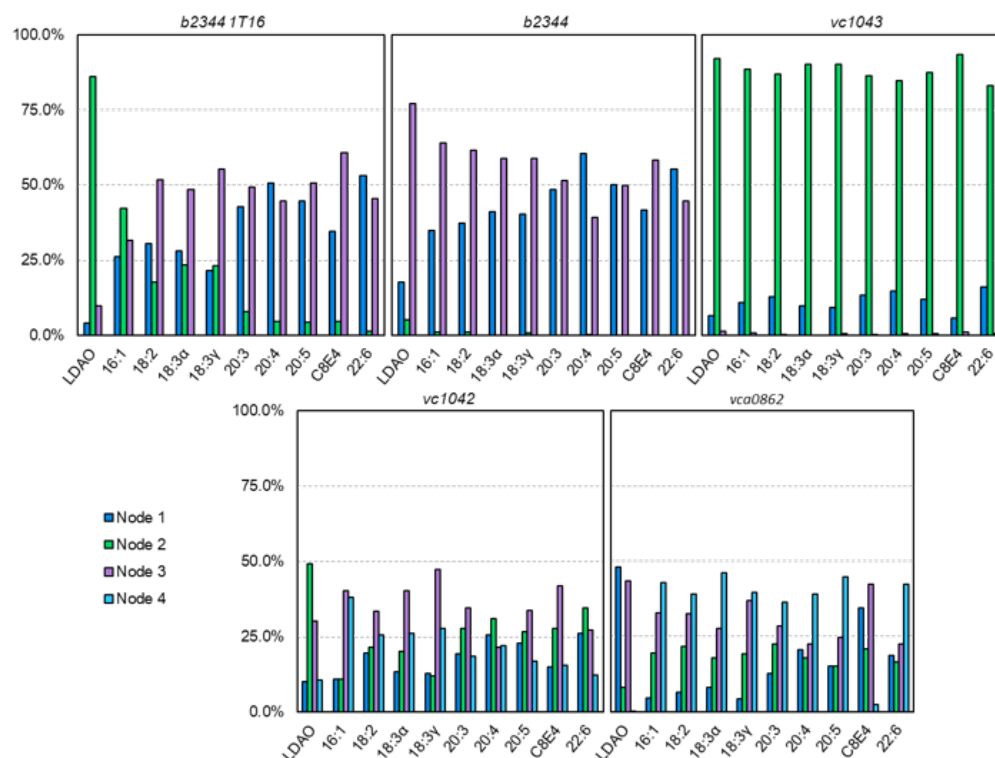


**Figure 7.** Charts of FAs by type located around certain nodes. The % is out of the 500 docked instances of each FA type over the 50 frame trajectory. The *b2334*, *b2334*, and *vc1043* docking resulted in three nodes, while *vc1042* and *vca0862* resulted in four nodes.

For the 1T16 test case, LDAO had a strong affinity for the high affinity binding pocket (Node 2) with 86.0% of the LDAO molecules docked appearing in or around the high affinity binding site. The other small molecules such as 16:1, 18:2, 18:3 $\alpha$ , and 18:3 $\gamma$  also showed clustering in the Node 2 region (42.2%, 17.8%, 23.4%, and 23.2%, respectively). This is reasonable due to the original 1T16 structure having a LDAO molecule bound to the high affinity binding site [27] (the Node 2 locus), where other similarly shorter chained FAs could also fit into the open pocket. Interestingly, the S3 kink (Node 3) tended to have more docked FAs than the low affinity binding site (Node 1) which may be due to the tubular cavity of the S3 kink region, providing more surface area for FAs to bind to than the more open low affinity binding site. Amongst all the FAs tested, the average docking binding energy for Nodes 1 and 3 of 1T16 were  $-8.975$  and  $-8.976$  kcal/mol, respectively, indicating a very close average binding energy. Examining 18:2 in specific, the binding energy of 18:2 with Node 1 was better ( $-9.29$  versus  $-8.97$  kcal/mol), but AutoDock propagated more 18:2 FAs on Node 3. This is likely due to the AutoDock algorithm finding it more difficult to dock the Node 1 area due to a smaller binding channel, even if the binding channel has a better binding energy. Another example of this phenomena is 22:6 having the best overall binding energy when it was found in the high affinity binding site ( $-12.65$  versus  $-9.73$  and  $-10.11$  kcal/mol), however, this only occurred with 1.4% of 22:6 dockings because the high affinity binding site was originally bound to LDAO—A shorter carbon chained molecule.

The equilibrated *b2344* docking revealed that the high affinity binding site had fewer dockings than the other sites. This indicates that due to the vacancy of FAs during simulation, that the high affinity binding site was smaller and did not dock many FAs. Further investigation revealed that small positional changes in the high affinity binding pocket residues—particularly ALA153, ILE155, and LEU200 impeded the binding pocket channel, and greatly reducing the ability for FAs to fit in the binding pocket. Unlike the high affinity binding site, the S3 kink did appear to have comparable binding between the crystal struc-

ture bound with detergents and the equilibrated structure. Additional investigation of the RMSD (data not shown) between the two S3 kink structures showed very small structural differences ( $<1.3 \text{ \AA}$ ) between the two molecules, indicating that there does not appear to be a conformational change in the S3 binding pocket, but instead a shift in the gated channel between the high affinity site and S3 kink as proposed by van den Berg [27]. The size and saturation of the FA did have an effect on the docking. Typically, the longer the FA carbon chains and more unsaturated, the affinity for Node 1 was increased and the affinity for Node 3 was decreased - mirroring the 1T16 dockings.

The *vc1042* docking revealed a visible main channel. It is predicted that the FAs move from Node 1 to Node 2 to Node 4 and then to Node 3, the S3 kink (Figure 6D). The clustering of FAs did not show much preference for any one of the four nodes with the exception of Node 3, where the totaled percent FAs located at Nodes 1, 2, 3, and 4 were 17.5%, 26.2%, 35.0%, and 21.3%, respectively. As expected of a *V. cholerae* homolog there was no discernable difference in FA tail length or saturation which is reasonable due to *V. cholerae*'s ability to uptake long-chain fatty acids.

In *vc1043*'s docking, Nodes 1 and 2 were in close proximity to one another as seen in Figure 6F, the major difference between the two being Node 2 is the locus of the high affinity binding site in the *E. coli* homolog. *vc1043* showed a strong favoritism for Node 2 with a total of 88.3% of all FAs appearing in the Node 2 region. Figure 6F illustrates the FA's tendency to funnel around Node 2. Only 0.6% of FAs were found in the S3 kink region (Node 3), alluding to a conformational mechanism to allow passage of the FA.

The docking of *vca0862* showed a high affinity for the outer portion of the S3 kink (Node 4). This is unexpected based on the premise that FAs travel through the beta barrel in *E. coli*. Node 4 does tend to have a more pronounced indentation making docking more ideal than some other locations; however, the docking did not factor in the lipopolysaccharide (LPS) which encompassed the outer perimeter of the FadL beta barrel, which would leave little room for FAs. AutoDock's current atom limit prevents a system with LPS included. These results indicate that the *vca0862* beta barrel was not in an open conformation for the 50 frames used for docking. This suggests that a conformational change may be necessary in order to allow a fatty acid to pass through. It is important to note that the lower C-score in the I-TASSER [26] folding,  $-1.08$ , may have a part in this resulting barrel structure, however, additional computational foldings and Molecular Dynamic runs using different programs (data not shown) were performed to test the viability of alternatively folded *vca0862* sequences; none of which had any notable differences in the structure.

### 3.6. Equilibrated *E. coli* b2344 Fatty Acids show Similar Channels as the X-ray Crystal Structure 1T16

To determine any important residues in the transport of FAs, the docked homologs were searched for any residues within  $3 \text{ \AA}$  of each of the docked FAs. These residues were agglomerated, and each residue found was counted for recurrences. The resulting table (Table 1) shows the twenty residues that were found to interact with the docked FAs most often.

For the *E. coli* b2344 homolog dockings, the residues found most frequently were those of the low affinity binding site and the S3 kink. This was expected, as the nodal analysis determined that the majority of FAs were docked in the Node 1 and 3 regions. While not in the same proportions, many of the same residues were found for both the b2344 1T16 and the equilibrated b2344 structures. Residues PRO253, ILE254, PRO255, and PHE315 have a reoccurring presence in the low affinity binding sites for both structures Figure 8A,C. Residues GLY2, LEU5, PRO54, VAL56, ALA74, GLY103, LEU104, ALA105, PRO362, and ARG366 are commonly found in the S3 kink region. The majority of these residues are nonpolar except for the polar glycines GLY2 and GLY103 and the positively charged arginine, ARG366. The arginine headgroup faces towards the S3 kink pocket indicating an affinity for carboxyl groups of FAs which is confirmed by the number of FA carboxyl headgroups in the proximity of ARG366 during docking. This could indicate an

orientation of FA with the tail group facing the outlet before egress of FA through the S3 kink. The RMSD for the heavy atoms of these residues tends to be between 1.1Å and 1.7Å, alluding to a stable S3 kink structure even with the difference of a bonded LDAO in the S3 kink of 1T16.

**Table 1.** Residue count for residues found within a 3 Å proximity of each FA for each frame. For each FadL homolog 100 FAs were docked for each of the 50 frames, giving a maximum residue count of 5000.

b2344 1T16		b2344		vc1042		vc1043		vca0862	
Proximity	Residue	Proximity	Residue	Proximity	Residue	Proximity	Residue	Proximity	Residue
2958	LEU104	2852	LEU104	2654	PHE3	4253	PHE108	2627	ALA102
2156	ARG366 **	2705	ALA105	2488	GLN4 *	3751	PHE3	2522	GLN74 *
2083	PHE3	2683	ARG366 **	2075	LEU5	3586	TRP300	1761	PRO72
2044	PRO54	2651	ALA74	1981	MET108	3415	TYR298 *	1732	SER119 *
1977	ALA74	2624	PRO54	1797	ARG339 **	3342	GLN4*	1716	LYS151 **
1943	ALA105	2331	PRO362	1709	PHE77	3249	LEU238	1501	VAL5
1910	PRO362	2274	ASP363 *	1646	PRO54	3182	TRP268	1498	VAL101
1849	LEU5	2178	GLY2 *	1626	VAL52	3074	ARG163 **	1456	VAL52
1789	VAL56	2154	LEU5	1568	VAL396	2858	MET161	1417	VAL76
1680	PHE315	2087	ILE361	1538	PRO335	2504	ILE274	1401	PRO54
1673	PRO255	2078	ILE52	1523	VAL56	2277	PRO241	1396	ILE121
1639	PRO253	2058	GLY103 *	1503	THR331 *	2187	VAL129	1237	ALA71
1626	GLY2 *	2049	PRO255	1491	TRP272	1697	VAL339	1168	ASP327 *
1623	ILE52	2006	GLN316 *	1462	VAL243	1588	LYS296 **	1137	ILE75
1594	GLY103 *	1965	PHE315	1418	THR244 *	1567	PHE276	1035	ARG330 **
1588	ARG157 **	1923	VAL56	1385	GLU336 *	1413	ILE266	1019	GLY100 *
1580	ILE254	1870	ILE254	1384	ALA1	1319	LEU240	1013	GLY2 *
1526	LYS317 **	1756	PRO75	1268	HSD79 **	1293	THR127 *	1004	THR103 *
1440	MET390	1673	PRO253	1231	ILE334	1272	SER338 *	977	ASP117 *
1426	ALA410	1643	ALA77	1187	MET241	1256	ALA330	943	ALA379

\* Polar, but neutral charged residue; \*\* Positively charged residues (pH 7).

### 3.7. *V. cholerae* vc1042 Docking Generates a Well Defined Transport Channel

The *V. cholerae* homolog *vc1042* residues were primarily centered around the predicted transport channel Figure 9B. This channel tends to start from between the 5th and 6th extracellular loops (Figure S6B). The FA is predicted to bypass the N-terminal hatch (residues 1 through 5), and then past the N-terminal hatch through the S3 kink opening. The N-terminal hatch in the docking does not appear to restrict transport in our model as it has been predicted for *E. coli* *b2344* [27,37], as the docked FAs revealed a continuous channel starting from the extracellular space around the 5th and 6th extracellular loops and ending at the S3 kink. This is somewhat unexpected as, generally, an FA transport protein would have some selection mechanism specific to FAs. The residues that line the predicted channel are primarily hydrophobic, with a few exceptions (GLN4, HSD79, THR244, THR331, GLU336, and ARG399) which are all hydrophilic (ARG339 also having a positive charge). These residues are placed periodically throughout the channel in such a way that it could be the FA headgroup's attraction to these residues that guide the movement of the FA through the channel—possibly in a orientation specific manner. The predicted channel appears to end at the S3 kink in the same manner as the *E. coli* homolog. A similar computational study involving the docking of the bottom half of the homologs (data not shown) revealed that there was a discontinuity from the main channel to any docking channels found in the bottom of the protein reinforcing the hypothesis that the S3 kink is the FA egress point [37]. Oddly, the predicted channel for *vc1042* shares a similar overlap of the *E. coli* homolog's high affinity binding site location and N-terminal hatch domain, but interestingly, the *vc1042* pathway bypasses the predicted hatch domain pathway used in *E. coli*. It is interesting that the original pathway (through the high affinity binding site location, and then through a tunnel created by a conformational mechanism occurring with the N-terminal hatch domain) may still exist somehow in the *V. cholerae* homolog. Whether or not this N-terminal hatch pathway is vestigial or is functional has yet to be determined at this time computationally or experimentally.

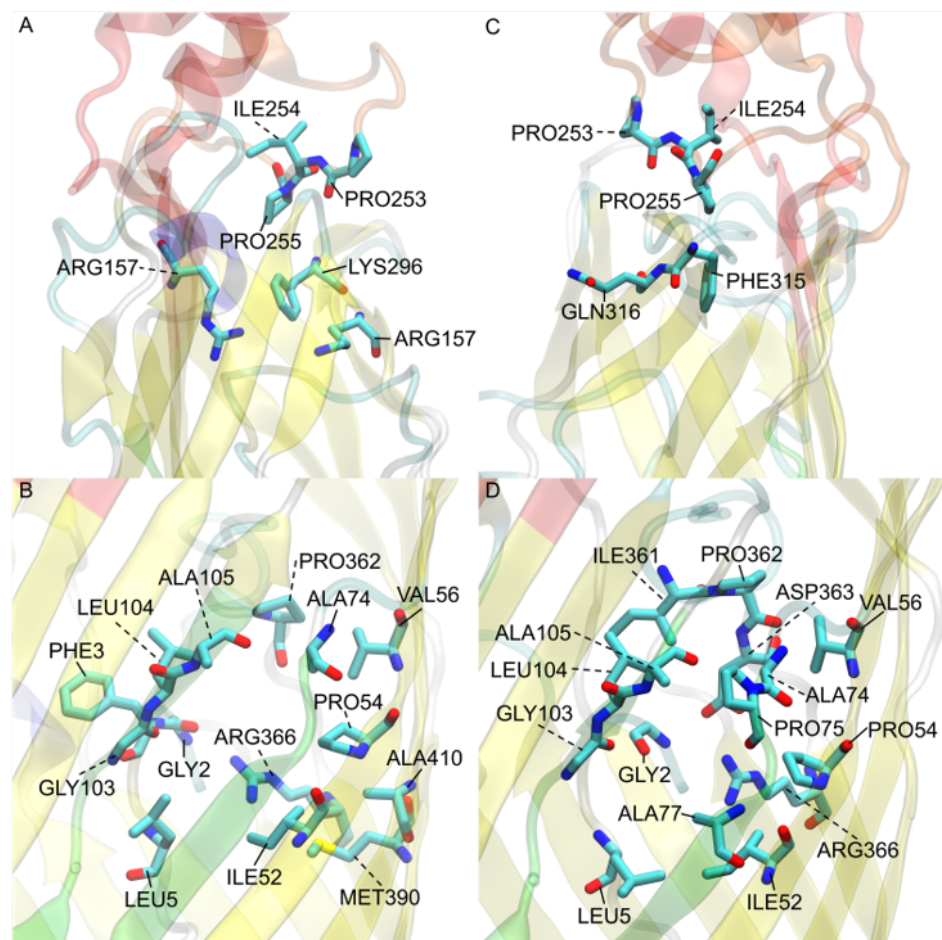


**Figure 8.** *E. coli* FadL binding residues of (A) 1T16 low affinity binding site residues, (B) 1T16 S3 kink, (C) *E. coli* low affinity binding site, and (D) *E. coli* S3 kink. The L3 loops are colored red, the L4 loops are colored orange, and the S3 kinks are colored green for reference. Perspective angles differ for easier observation of residues.

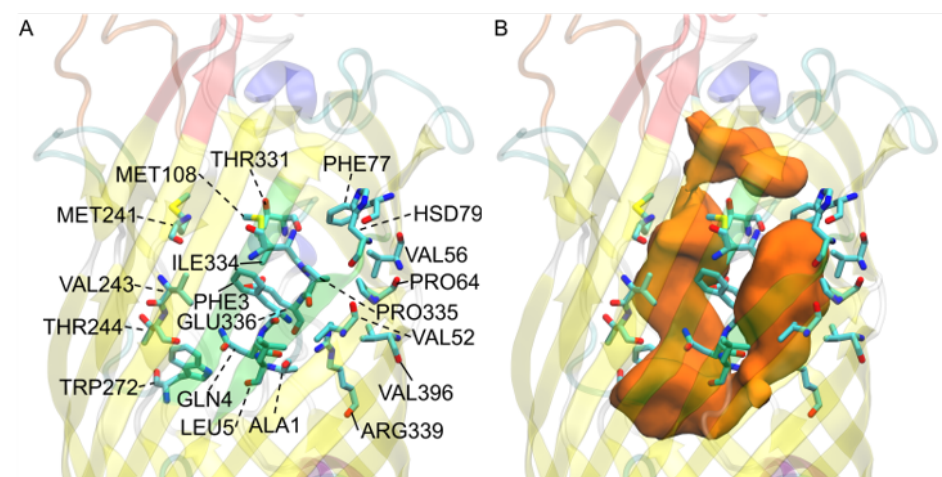


**Figure 9.** *V. cholerae* vc1042 FA interacting residues: (A) residue names and locations; (B) predicted transport channel shown from a surface view of all docked FAs (orange) shown with its relation to the displayed residues. The L3 loops is colored red, the L4 loop is colored orange, and the S3 kink is colored green for reference.

### 3.8. *V. cholerae* *vc1043* Transport Channel Has a Discontinuity Revealing Multiple Predicted Pathways

*V. cholerae* homolog *vc1043* was found to have a very large flat channel that seems to funnel FAs to the N-terminal hatch domain (Figure 10). The entry of the channel can be seen in the supplemental material (Figure S6C) where the undefined low affinity binding region is again found between the base of the extracellular loops. The channel leads to the N-terminal hatch opposite the S3 kink. The N-terminal hatch domain rests in the same position as the *E. coli* 1T16 structure and the channel overlaps the general area of the high affinity binding. This could indicate an evolutionary adaptation to combine the low affinity and the high affinity binding sites found in *b2344* favoring a more direct pathway, but leaving the mechanisms of the N-terminal hatch domain—which would play the same role for the *vc1043* homolog as it does for the *E. coli* homolog. This would require the N-terminal domain to act as a hatch that opens and closes for FA transport, unfortunately this mechanism at the atomistic level has not been elucidated for accurate prediction. Alternatively, the *vc1043* channel spans further down than the transposed high affinity binding site ending below the N-terminal hatch and opposite the S3 kink. This could be an alternate pathway that follows the *vc1042* pathway, but with some selection mechanism to cross the remainder of the channel. Again, this proposed pathway has yet to be substantiated from experimentation or computational study. The docked FAs did not appear in the S3 kink pore, likely due to LYS130 from the fourth beta strand, S4, positioned parallel to the S3 kink that appears to be attracted to GLU50, SER106, and ASN107 as well as the backbone oxygens of the S3 kink residue GLY109. This attraction causes LYS130 to fill the S3 transport pore and prevent docking (and possibly FA transport). This could be a selection mechanism that may determine the resulting FA position or FA type. The channel of *vc1043* was found to be composed generally of hydrophobic residues. The exceptions to this are GLN4, THR127, TYR298, and SER338 which are hydrophilic, and ARG163 and LYS296 which are positively charged. Previously, it was postulated that the hydrophilic residues in *vc1042* guided the FAs through the channel through hydrophilic residue interactions, but *vc1043* hydrophilic residues are restricted to the top of the conical channel. Therefore, there are no hydrophilic residues present in the vacant channel to guide the polar FA headgroup through the channel. It is predicted that the polar head groups bind to the hydrophilic residues at the top of the channel for alignment. Directional positioning of the FA is yet to be determined experimentally or in any *in silico* study, but FA orientation may play an important role with a positively charged lysine (LYS130) residue blocking the S3 kink pore.

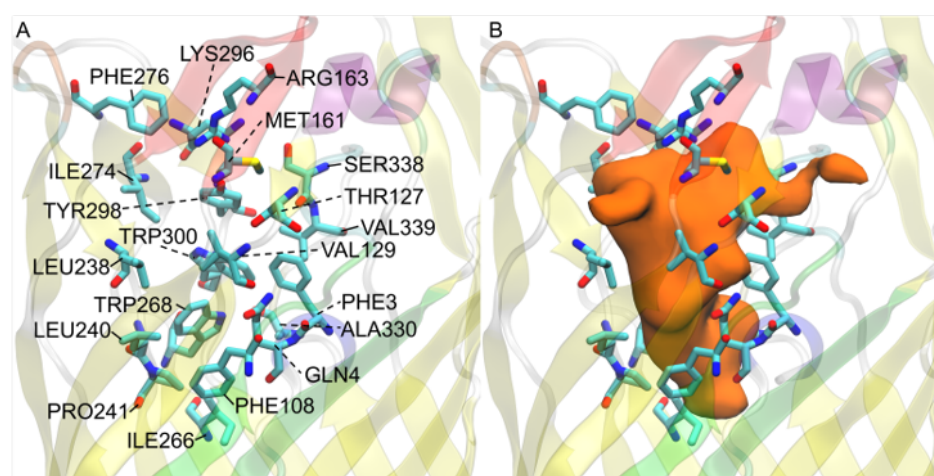


**Figure 10.** *V. cholerae* *vc1043* FA interacting residues: (A) residue names and locations; (B) predicted transport channel shown from a surface view of all docked FAs (orange) shown with its relation to the displayed residues. The L3 loops is colored red, the L4 loop is colored orange, and the S3 kink is colored green for reference.

### 3.9. *V. cholerae* vca0862 Docking Reveals a Transport Channel External to the Beta Barrel

The docking of *V. cholerae* homolog vca0862 revealed that the majority of docking sites did not occur within the computationally folded and equilibrated beta barrel structure of the FadL protein, but rather along the outer barrel primarily around the S3 kink (Figure 11B). This appears to be due to the substantial lack of open space for FAs to be docked on the inner portion of the beta barrel. Oddly, there seems to be a pathway from between the L3 and L4 loops that goes down the side of the protein and to the outside of the S3 kink as shown in the supplemental material (Figure S7). The results implicate that any molecule of similar size to a FA would be able to make its way through the side channel unless there was some interplay with the interface of the LPS and lipid bilayer to create some sort of selectivity mechanism. The channel between the outer portion of the S3 kink and the predicted initial binding sites between the L3 and L4 extracellular loops tends to close off depending on the L3 and L4 conformations. These L3 and L4 conformations may be the selectivity mechanism that this homolog uses to ensure the uptake of FAs instead of bactericidal compounds. Many of the docked FA were found within the S3 kink, where the internal cavity of the S3 kink would be vestigial if the FAs are transported to the predicted egress point without entry of the FA into the FadL beta barrel structure. Unless the s3 kink has an orientation mechanism to help FAs diffuse passively through the membrane. This vestigial S3 kink cavity agrees with the secondary docking of the bottom portion of the protein, where no FA pathways were found from the S3 kink to the periplasmic end of the FadL protein.

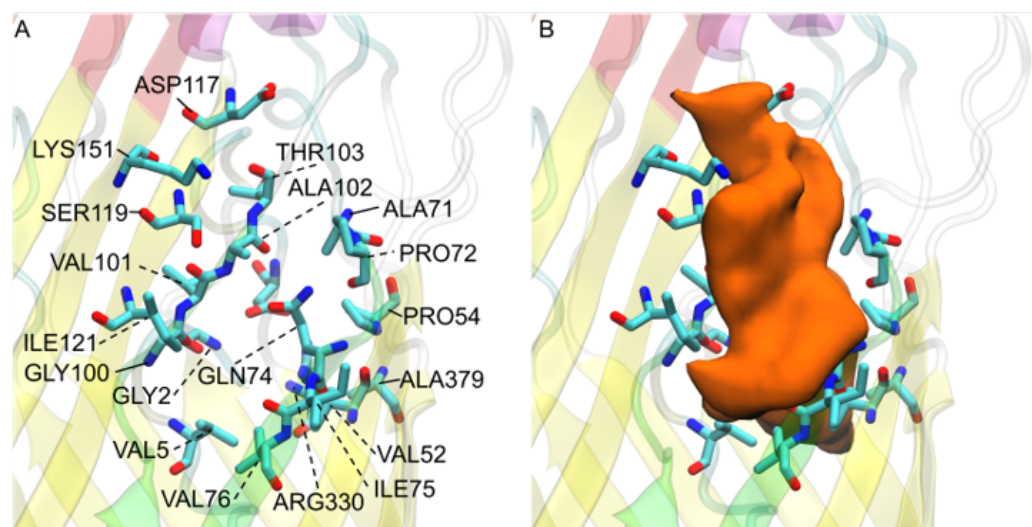


**Figure 11.** *V. cholerae* vca0862 FA interacting residues: (A) residue names and locations; (B) observed transport channel shown from a surface view of all docked FAs (orange) shown with its relation to the displayed residues. The L3 loops is colored red, the L4 loop is colored orange, and the S3 kink is colored green for reference.

### 3.10. Simulations and Docking Agree the S3 Kink Is the Fatty Acid Point of Egress

To verify that the S3 kink is the egress point first suggested by Hearn et al. [37], the membrane layer location after equilibration was checked for the possibility of membrane diffusion. The resulting lipid bilayer headgroups or the polar heavy atoms of the LPS were shown in relation to the D3 kink pore (Figure 12). This pore was typically found at the upper portion of the LPS polar region indicating a strong affinity for the polar headgroups of the FA with the polar LPS residues, indicating a good possibility for assimilation into the LPS bilayer and passive diffusion into the periplasmic space. Additional docking studies (not shown) using the bottom portion of the FadL structures also revealed no such pathways through the lower portion of the N-terminus loop that fills the lower beta barrel for either *V. cholerae* or *E. coli*.

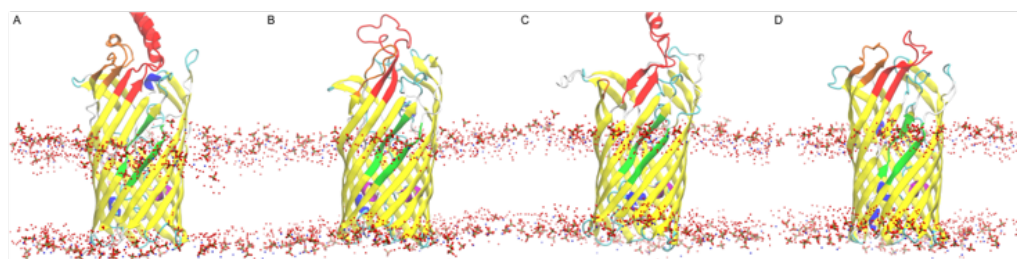


**Figure 12.** Lipid bilayer polar atom locations with respect to the: (A) *b2344*; (B) *vc1042*; (C) *vc1043*; and (D) *vca0862* FadL proteins after equilibration and docking.

### 3.11. Docking Energies Show that Binding is Stronger in the Presence of Fatty Acids

Ten docking conformations were produced per ligand creating a total of 100 docking conformations per FadL homolog frame. With 250 frames docked, 25,000 conformations were generated overall. The best conforming (lowest energy) are shown in Table S4. Similarly, the averaged docking energies by FA are given in Table S5.

Simulated docking results indicate that the original crystal structure *E. coli* 1T16 tended to have the most energetically favorable docking with respect to overall average as well as the best individual FA docking conformations. This is likely because the 1T16 structure was generated with the FadL protein bound with LDAO and C8E4 in the structure when the PDB was generated, giving it the specific conformation needed for strong binding. It is also apparent that the docking energies are more favorable for the longer chain FAs (with exception to C8E4 which has a total length of 21 heavy atoms). This result is likely due to the fact that longer FA chains provide more surface area for binding. However, many of the longer chained polyunsaturated FAs tend to have a hairpin tail due to the cis unsaturated portions. The uptake of these longer chained FAs would likely require some internal mechanisms for FA uptake that compensates for these rigid sections of the FAs, although these compensation mechanisms have not been found computationally.

## 4. Discussion

The atomistic study of FadL homologs reveals the structure and transport channels of *V. cholerae* homologs *vc1042*, *vc1043*, and *vca0862*. The *E. coli* controls showed agreeable results when compared the X-ray crystallography study [27]. All homologs tended to share similarity in their low affinity binding site locus at the base of the L3 and L4 extracellular loops, but the structure of extracellular loops themselves tended to deviate from the original template. The reason for the deviations has yet to be determined, but it may have an effect on nascent protein passage through the cell membrane, localization of the protein in the membrane with respect to the LPS, or as guide for FAs into to the transport channel.

The equilibration of *b2344* in comparison to the X-ray structure (1T16) shows that there are conformational shifts in the binding sites for FAs that are closed without the presence of FAs. *vc1043* shows this similarity, where it appears the presence of FA are required for the span between the observed channel and the S3 kink domain to activate and allow passage. The trajectories over 50 nanoseconds gives a wide range of conformations for the FA to propagate on the proteins, and for neither *b2344* or *vc1043* to reveal a contiguous channel through docking emphasizes the importance of the FA-protein interaction. This is not the case with *vc1042*, where the channel is fully expressed without FAs being present. The N-terminal hatch residues ALA1, GLY2, PHE3, and GLN4 were conserved throughout all of the homologs, as well as their tertiary structures and positions. These residues may play a part in conformational changes that allow selective passage of FAs through the cell [27,37]. However, the channels presented for the *V. cholerae* homolog *vc1042* suggests the possibility that this structure can be vestigial in the transport of FAs, but retain the conserved sequence as part of the signal peptide sequence [38], the protease recognizing the signal sequence ALA-GLY-PHE-GLN as part of the processing site. This is subject to the protease responsible for the cleavage, which is has not been discovered at this time.

The resulting structure of *vca0862* shows that the channel is on the exterior of the beta barrel. This may be due to the folded structure, but multiple foldings and equilibrations across different software did not predict any significant differences in the structure. Investigation using RefSeq [39] on FA uptake revealed that *V. cholerae* strains that have these homologs all contain a copy of *vc1042*, *vc1043*, (chromosome I) and *vca0862* (chromosome II) (data not shown). *vca0862* has not been shown in any studies to be the definitive protein responsible for FA transport, with many bioinformatic searches of FadL neglecting *vc1042* and *vc1043*. Additionally, in studies with gene expression of *V. cholerae* strain N16961 between in vitro and in vivo, the expression of *vca0862* was low compared to the other FadL sequences [40]. The relatively low expression of *vca0862* and the lack of a suitable channel for FA transfer may indicate that this protein may be a result of a loss of function adaptation [41]. Interestingly the data presented by Xu et al. reveals that expression of *vc1042* increases in vivo (in rabbits) in comparison to in vitro (growth in LB). The inverse was true for *vc1043* with a reduction in expression in vivo. The effect of FA concentration in the lumen as opposed to the FA devoid LB, may be a selection mechanism for *vc1042* which appears to have a larger, more complete, and less selective channel.

The atomistic structures of *Vibrio cholerae* FadL homologs were found and analyzed. The channels of these homologs bring to light the complex nature of biological systems and the diverse machinery that is used to adapt to environmental conditions. While each homolog has unique characteristics, the exact nature of each homolog is still unknown, and additional studies into these characteristics will shed light on the diversification and expanded uptake capacity for not only *Vibrio* species, but the growing list of Gram-negative bacteria demonstrating fatty acid utilization versatility.

**Supplementary Materials:** The following supporting information can be downloaded at: <https://www.mdpi.com/article/10.3390/biom12091269/s1>, Figure S1: I-TASSER folded structures. (A) the *E. coli* b2344 1T16 crystal structure compared to (B) *vc1042* (C), *vc1043*, and (D) *vca0862*. L3 and L4 loops are colored red and orange respectively, and the S3 kink is green for reference. (E-H) are views of the N-terminal hatch domain (blue) for *E. coli* b2344, *vc1042*, *vc1043*, and *vca0862* respectively. Figure S2: AlphaFold generated structures. The structures are colored by pLDDT scaling from 100 (blue) to 90 (white). Any residues that were below 90 were colored red. The only residues that had a pLDDT value of less than 80 were in the extracellular loops with the exception of ALA1 in homolog *vc1043* with a pLDDT of 78.75. Figure S3: Aligned backbone structures generated by I-TASSER (green) and AlphaFold (blue). The red line indicates the approximate location of the start of the extracellular loops. Figure S4: 2-D representations of constituents of the *V. cholerae* membranes. Figure S5: RMSD of equilibrated systems over the 250 ns trajectory. Figure S6: Surface view of FA transport channel entrance points (shown in purple) for (A) b2344, (B) *vc1042*, (C) *vc1043* FadL proteins after equilibration. The general protein surface is colored by secondary structure and the L3 and L4 loops are colored red and orange respectively. This perspective is opposite of the S3 kink. Figure S7. Surface view of FA exterior pathway (shown in purple) for *vca0862* FadL protein after equilibration. The general protein surface is colored by secondary structure, the S3 kink is colored green, and the L3 and L4 loops are colored red and orange respectively. Table S1: Fatty acids tested during docking. Table S2: Ramachandran Z-Scores. Table S3: RMSD of Initial I-TASSER and AlphaFold Backbone Structures. Table S4: Best Conformation Energies (most negative) from Docking (energy units in kcal/mol). Table S5: Overall Average Conformation Energy from Docking (energy units in kcal/mol).

**Author Contributions:** Conceptualization, A.T, L.M., D.G. and B.H.; Data curation, A.T., L.M. and B.H.; Formal analysis, A.T.; Funding acquisition, D.G. and B.H.; Investigation, A.T.; Methodology, A.T. and L.M.; Project administration, L.M. and B.H.; Resources, D.G. and B.H.; Software, A.T. and B.H.; Supervision, D.G. and B.H.; Validation, A.T., L.M., D.G. and B.H.; Visualization, A.T.; Writing—original draft, A.T.; Writing—review & editing, A.T., L.M., D.G. and B.H. All authors have read and agreed to the published version of the manuscript.



**Funding:** We thank the support of NSF REU #1852042 and #2149956, and the internal support from the Department of Computer Science and Engineering and the Office of the Vice Chancellor of Research at the University of Tennessee at Chattanooga.

**Institutional Review Board Statement:** Not applicable.

**Informed Consent Statement:** Not applicable.

**Data Availability Statement:** The data presented in this study are available on request from the corresponding author.

**Conflicts of Interest:** The authors declare no conflict of interest.

## References

1. Nunn, W.D. A molecular view of fatty acid catabolism in *Escherichia coli*. *Microbiol. Rev.* **1986**, *50*, 179–192. [[CrossRef](#)] [[PubMed](#)]
2. Nunn, W.D.; Simons, R.W. Transport of long-chain fatty acids by *Escherichia coli*: Mapping and characterization of mutants in the *fadL* gene. *Proc. Natl. Acad. Sci. USA* **1978**, *75*, 3377–3381. [[CrossRef](#)] [[PubMed](#)]
3. Black, P.N.; Said, B.; Ghosn, C.R.; Beach, J.V.; Nunn, W.D. Purification and characterization of an outer membrane-bound protein involved in long-chain fatty acid transport in *Escherichia coli*. *J. Biol. Chem.* **1987**, *262*, 1412–1419. [[CrossRef](#)]
4. de Carvalho, C.; Caramujo, M.J. The Various Roles of Fatty Acids. *Molecules* **2018**, *23*. [[CrossRef](#)]
5. Abedi, E.; Sahari, M.A. Long-chain polyunsaturated fatty acid sources and evaluation of their nutritional and functional properties. *Food Sci. Nutr.* **2014**, *2*, 443–463. [[CrossRef](#)]
6. Leonard, A.E.; Pereira, S.L.; Sprecher, H.; Huang, Y.S. Elongation of long-chain fatty acids. *Prog. Lipid Res.* **2004**, *43*, 36–54. [[CrossRef](#)]
7. Berge, J.P.; Barnathan, G. Fatty acids from lipids of marine organisms: Molecular biodiversity, roles as biomarkers, biologically active compounds, and economical aspects. *Adv. Biochem. Eng. Biotechnol.* **2005**, *96*, 49–125. [[CrossRef](#)]
8. Harwood, J.L.; Guschina, I.A. The versatility of algae and their lipid metabolism. *Biochimie* **2009**, *91*, 679–684. [[CrossRef](#)]
9. Jimenez-Diaz, L.; Caballero, A.; Segura, A. Pathways for the Degradation of Fatty Acids in Bacteria. In *Aerobic Utilization of Hydrocarbons, Oils and Lipids*; Springer: Berlin/Heidelberg, Germany, 2017; pp. 1–23. [[CrossRef](#)]
10. Ernst, R.; Ejsing, C.S.; Antonny, B. Homeoviscous Adaptation and the Regulation of Membrane Lipids. *J. Mol. Biol.* **2016**, *428*, 4776–4791. [[CrossRef](#)]
11. Zhang, Y.M.; Rock, C.O. Membrane lipid homeostasis in bacteria. *Nat. Rev. Microbiol.* **2008**, *6*, 222–233. [[CrossRef](#)]
12. Cronan, J.E.; Thomas, J. Bacterial Fatty Acid Synthesis and its Relationships with Polyketide Synthetic Pathways. *Methods Enzymol.* **2009**, *459*, 395–433. [[CrossRef](#)]
13. Parsons, J.B.; Rock, C.O. Is bacterial fatty acid synthesis a valid target for antibacterial drug discovery? *Curr. Opin. Microbiol.* **2011**, *14*, 544–549. [[CrossRef](#)] [[PubMed](#)]
14. Yao, J.; Rock, C.O. Exogenous fatty acid metabolism in bacteria. *Biochimie* **2017**, *141*, 30–39. [[CrossRef](#)] [[PubMed](#)]
15. Ginsburgh, C.L.; Black, P.N.; Nunn, W.D. Transport of long chain fatty acids in *Escherichia coli*. Identification of a membrane protein associated with the *fadL* gene. *J. Biol. Chem.* **1984**, *13*, 8437–8443. [[CrossRef](#)]
16. Weimar, J.D.; DiRusso, C.C.; Delio, R.; Black, P.N. Functional role of fatty acyl-coenzyme A synthetase in the transmembrane movement and activation of exogenous long-chain fatty acids. Amino acid residues within the ATP/AMP signature motif of *Escherichia coli* FadD are required for enzyme activity and fatty acid transport. *J. Biol. Chem.* **2002**, *277*, 29369–29376. [[CrossRef](#)]
17. Giles, D.K.; Hankins, J.V.; Guan, Z.; Trent, M.S. Remodelling of the *Vibrio cholerae* membrane by incorporation of exogenous fatty acids from host and aquatic environments. *Mol. Microbiol.* **2011**, *79*, 716–728. [[CrossRef](#)]
18. Hobby, C.R.; Herndon, J.L.; Morrow, C.A.; Peters, R.E.; Symes, S.J.K.; Giles, D.K. Exogenous fatty acids alter phospholipid composition, membrane permeability, capacity for biofilm formation, and antimicrobial peptide susceptibility in *Klebsiella pneumoniae*. *Microbiologyopen* **2019**, *8*, e00635. [[CrossRef](#)]
19. Eder, A.E.; Munir, S.A.; Hobby, C.R.; Anderson, D.M.; Herndon, J.L.; Siv, A.W.; Symes, S.J.K.; Giles, D.K. Exogenous polyunsaturated fatty acids (PUFAs) alter phospholipid composition, membrane permeability, biofilm formation and motility in *Acinetobacter baumannii*. *Microbiology* **2017**, *163*, 1626–1636. [[CrossRef](#)]
20. Baker, L.Y.; Hobby, C.R.; Siv, A.W.; Bible, W.C.; Glennon, M.S.; Anderson, D.M.; Symes, S.J.; Giles, D.K. *Pseudomonas aeruginosa* responds to exogenous polyunsaturated fatty acids (PUFAs) by modifying phospholipid composition, membrane permeability, and phenotypes associated with virulence. *BMC Microbiol.* **2018**, *18*, 117. [[CrossRef](#)]
21. Herndon, J.L.; Peters, R.E.; Hofer, R.N.; Simmons, T.B.; Symes, S.J.; Giles, D.K. Exogenous polyunsaturated fatty acids (PUFAs) promote changes in growth, phospholipid composition, membrane permeability and virulence phenotypes in *Escherichia coli*. *BMC Microbiol.* **2020**, *20*, 305. [[CrossRef](#)]
22. Moravec, A.R.; Siv, A.W.; Hobby, C.R.; Lindsay, E.N.; Norbash, L.V.; Shults, D.J.; Symes, S.J.K.; Giles, D.K. Exogenous Polyunsaturated Fatty Acids Impact Membrane Remodeling and Affect Virulence Phenotypes among Pathogenic *Vibrio* Species. *Appl. Environ. Microbiol.* **2017**, *83*, e01415-17. [[CrossRef](#)] [[PubMed](#)]
23. van Berge Henegouwen, G.P.; van der Werf, S.D.J.; Ruben, A.T. Fatty acid composition of phospholipids in bile in man: Promoting effect of deoxycholate on arachidonate. *Clin. Chim. Acta* **1987**, *165*, 27–37. [[CrossRef](#)]

24. Pride, A.C.; Guan, Z.; Trent, M.S. Characterization of the *Vibrio cholerae* VolA surface-exposed lipoprotein lysophospholipase. *J. Bacteriol.* **2014**, *196*, 1619–1626. [[CrossRef](#)] [[PubMed](#)]
25. Altschul, S.F.; Gish, W.; Miller, W.; Myers, E.W.; Lipman, D.J. Basic local alignment search tool. *J. Mol. Biol.* **1990**, *215*, 403–410. [[CrossRef](#)]
26. Yang, J.; Yan, R.; Roy, A.; Xu, D.; Poisson, J.; Zhang, Y. The I-TASSER Suite: Protein structure and function prediction. *Nat. Methods* **2015**, *12*, 7–8. [[CrossRef](#)]
27. van den Berg, B.; Black, P.N.; Clemons, W.M.J.; Rapoport, T.A. Crystal structure of the long-chain fatty acid transporter FadL. *Science* **2004**, *304*, 1506–1509. [[CrossRef](#)] [[PubMed](#)]
28. Jumper, J.; Evans, R.; Pritzel, A.; Green, T.; Figurnov, M.; Ronneberger, O.; Tunyasuvunakool, K.; Bates, R.; Zidek, A.; Potapenko, A.; et al. Highly accurate protein structure prediction with AlphaFold. *Nature* **2021**, *596*, 583–589. [[CrossRef](#)]
29. Mirdita, M.; Schütze, K.; Moriawaki, Y.; Heo, L.; Ovchinnikov, S.; Steinegger, M. ColabFold: Making Protein folding accessible to all. *Nat. Methods* **2022**, *19*, 679–682. [[CrossRef](#)]
30. Williams, C.J.; Headd, J.J.; Moriarty, N.W.; Prisant, M.G.; Videau, L.L.; Deis, L.N.; Verma, V.; Keedy, D.A.; Hintze, B.J.; Chen, V.B.; et al. MolProbity: More and better reference data for improved all-atom structure validation. *Protein Sci.* **2018**, *27*, 293–315. [[CrossRef](#)]
31. Wu, E.L.; Cheng, X.; Jo, S.; Rui, H.; Song, K.C.; Davila-Contreras, E.M.; Qi, Y.; Lee, J.; Monje-Galvan, V.; Venable, R.M.; et al. CHARMM-GUI Membrane Builder toward realistic biological membrane simulations. *J. Comput. Chem.* **2014**, *35*, 1997–2004. [[CrossRef](#)]
32. Phillips, J.C.; Braun, R.; Wang, W.; Gumbart, J.; Tajkhorshid, E.; Villa, E.; Chipot, C.; Skeel, R.D.; Kale, L.; Schulten, K. Scalable molecular dynamics with NAMD. *J. Comput. Chem.* **2005**, *26*, 1781–1802. [[CrossRef](#)] [[PubMed](#)]
33. Brooks, B.R.; Brooks, C.L.; Mackerell, A.D.J.; Nilsson, L.; Petrella, R.J.; Roux, B.; Won, Y.; Archontis, G.; Bartels, C.; Boresch, S.; et al. CHARMM: The biomolecular simulation program. *J. Comput. Chem.* **2009**, *30*, 1545–1614. [[CrossRef](#)] [[PubMed](#)]
34. Darden, T.; York, D.; Pedersen, L. Particle mesh Ewald: AnN log(N) method for Ewald sums in large systems. *J. Chem. Phys.* **1993**, *98*, 10089–10092. [[CrossRef](#)]
35. Morris, G.M.; Huey, R.; Lindstrom, W.; Sanner, M.F.; Belew, R.K.; Goodsell, D.S.; Olson, A.J. AutoDock4 and AutoDockTools4: Automated docking with selective receptor flexibility. *J. Comput. Chem.* **2009**, *30*, 2785–2791. [[CrossRef](#)] [[PubMed](#)]
36. McNutt, A.T.; Francoeur, P.; Aggarwal, R.; Masuda, T.; Meli, R.; Ragoza, M.; Sunseri, J.; Koes, D.R. GNINA 1.0: Molecular docking with deep learning. *J. Cheminform.* **2021**, *13*, 43. [[CrossRef](#)]
37. Hearn, E.M.; Patel, D.R.; Lepore, B.W.; Indic, M.; van den Berg, B. Transmembrane passage of hydrophobic compounds through a protein channel wall. *Nature* **2009**, *458*, 367–370. [[CrossRef](#)]
38. Black, P.N. Primary sequence of the *Escherichia coli* fadL gene encoding an outer membrane protein required for long-chain fatty acid transport. *J. Bacteriol.* **1991**, *173*, 435–442. [[CrossRef](#)]
39. O’Leary, N.A.; Wright, M.W.; Brister, J.R.; Ciufu, S.; Haddad, D.; McVeigh, R.; Rajput, B.; Robbertse, B.; Smith-White, B.; Ako-Adjei, D.; et al. Reference sequence (RefSeq) database at NCBI: Current status, taxonomic expansion, and functional annotation. *Nucleic Acids Res.* **2016**, *44*, D733–D745. [[CrossRef](#)]
40. Xu, Q.; Dziejman, M.; Mekalanos, J.J. Determination of the transcriptome of *Vibrio cholerae* during intractintestinal growth and midexponential phase in vitro. *Proc. Natl. Acad. Sci. USA* **2003**, *100*, 1286–1291. [[CrossRef](#)]
41. Hottes, A.K.; Freddolino, P.L.; Khare, A.; Donnell, Z.N.; Liu, J.C.; Tavazoie, S. Bacterial adaptation through loss of function. *PLoS Genet.* **2013**, *9*, e1003617. [[CrossRef](#)]